

IMAGING OBSERVATIONS OF QUASI-PERIODIC PULSATIONS IN SOLAR FLARE LOOPS WITH SDO/AIA

J. T. SU¹, Y. D. SHEN², Y. LIU², Y. LIU³, AND X. J. MAO^{1,4}

¹ Key Laboratory of Solar Activity, National Astronomical Observatories, Chinese Academy of Science, Beijing 100012, China

² National Astronomical Observatories/Yunnan Observatory, Chinese Academy of Sciences, Kunming 650011, China

³ W. W. Hansen Experimental Physical Laboratory, Stanford University, Stanford, CA 94305, USA

⁴ Department of Astronomy, Beijing Normal University, Beijing 100875, China

Received 2012 March 20; accepted 2012 June 13; published 2012 August 1

ABSTRACT

Quasi-periodic pulsations (QPPs) of flaring emission with periods from a few seconds to tens of minutes have been widely detected from radio bands to γ -ray emissions. However, in the past the spatial information of pulsations could not be utilized well due to the instrument limits. We report here imaging observations of the QPPs in three loop sections during a C1.7 flare with periods of $P = 24$ s–3 minutes by means of the extreme-ultraviolet 171 Å channel of the Atmospheric Imaging Assembly (AIA) instrument on board the *Solar Dynamics Observatory*. We confirm that the QPPs with the shortest period of 24 s were not of an artifact produced by the Nyquist frequency of the AIA 12 s cadence. The QPPs in the three loop sections were interconnected and closely associated with the flare. The detected perturbations propagated along the loops at speeds of 65–200 km s^{−1}, close to those of acoustic waves in them. The loops were made up of many bright blobs arranged in alternating bright and dark changes in intensity (spatial periodical distribution) with the wavelengths 2.4–5 Mm (as if they were magnetohydrodynamic waves). Furthermore, in the time–distance diagrams, the detected perturbation wavelengths of the QPPs are estimated to be ~ 10 Mm, which evidently do not fit the above ones of the spatial periodic distributions and produce a difference of a factor of 2–4 with them. It is suggested that the short QPPs with periods $P < 60$ s were possibly sausage-mode oscillations and the long QPPs with periods $P > 60$ s were the higher (e.g., >2nd) harmonics of slow magnetoacoustic waves.

Key words: Sun: activity – Sun: corona – Sun: flares – Sun: oscillations

Online-only material: color figures

1. INTRODUCTION

Quasi-periodic pulsations (QPPs) are a common feature of flaring energy releases in the solar atmosphere ranging in a wide band from radio to hard X-ray frequency, even extending to γ -rays (Nakariakov et al. 2010). The periods of QPPs vary from very fast (<0.5 s), to short period (0.5–5 s), to long period (>5 s) (Aschwanden 2003). A more practical classification would be short QPPs (sub-second), medium QPPs (seconds to several minutes), and long QPPs (from several to tens of minutes) according to the possible physical mechanism (Nakariakov & Melnikov 2009; Kupriyanova et al. 2010). The short ones are likely to be associated with the interactions of electromagnetic, plasma, or whistler waves with accelerated particles, detected in the radio emission (see, e.g., Aschwanden 1987), whereas the long ones are usually relevant to active region (AR) dynamics and global oscillations of the Sun, detected in radio, microwave, white-light, and X-ray emissions (e.g., Foullon et al. 2005; Nakariakov et al. 2006; Ofman & Sui 2006; Mészárosová et al. 2006; Li & Gan 2008; Zimovets & Struminsky 2009; Sych et al. 2009; Tan et al. 2010). The medium QPPs are likely related to magnetohydrodynamic (MHD) processes in solar flaring loops, also detected in radio, microwave, white-light, and X-ray emissions (e.g., Kliem et al. 2000; Inglis et al. 2008; Jakimiec & Tomczak 2008; Asai et al. 2001; Melnikov et al. 2005; Reznikova et al. 2007; McAteer et al. 2005; Inglis & Nakariakov 2009; Rao et al. 2010). More recently, they were also found in the high-energy part of the spectrum, γ -rays, with a period of about 40 s in a single X-class flare loop (Nakariakov et al. 2010). The fundamental physical processes in flares are relevant to spontaneous and triggered energy releases,

magnetic reconnection, thermodynamics, MHD oscillations, particle acceleration, and other kinetic effects (Nakariakov & Melnikov 2009).

Identification of physical mechanisms responsible for QPP events is a difficult task. In this point, imaging observations are very helpful to us, which may allow one to distinguish between different mechanisms responsible for the observed QPPs and thus reduce significantly the numbers of possible interpretations of the observed QPP event. The first attempt to utilize spatial information for pulsations was in the case of a single flaring loop undertaken by Nakariakov et al. (2003) and Melnikov et al. (2005). They found the possibility of the simultaneous existence of two modes of oscillations in the loop: the global sausage mode, with a period of $P_1 = 14\text{--}17$ s, and nodes at the footpoints, along with a higher harmonic (possibly with the radial wave number $l > 1$), with $P_2 = 8\text{--}11$ s. So far, extreme-ultraviolet (EUV) bands have exhibited better performance in coronal observations in obtaining spatial information than in other bands. For example, people have found MHD waves in the corona with EUV observations through *SoHO*, *TRACE*, and *Hinode* satellites (e.g., Ofman et al. 1997; Wang et al. 2009; King et al. 2003; Berghmans & Clette 1999; McIntosh et al. 2008; Marsh et al. 2009; Banerjee et al. 2009). Recently, with the Atmospheric Imaging Assembly (AIA; Lemen et al. 2012) on board the newly launched *Solar Dynamics Observatory* (*SDO*) with high cadences up to 12 s being put into use, this makes it possible for us to detect much faster coronal transient features (e.g., QPPs and short period waves) in EUV imaging observations. For example, Liu et al. (2011) have first detected fast coronal waves with a short period of 43 s through AIA 171 Å running difference images.

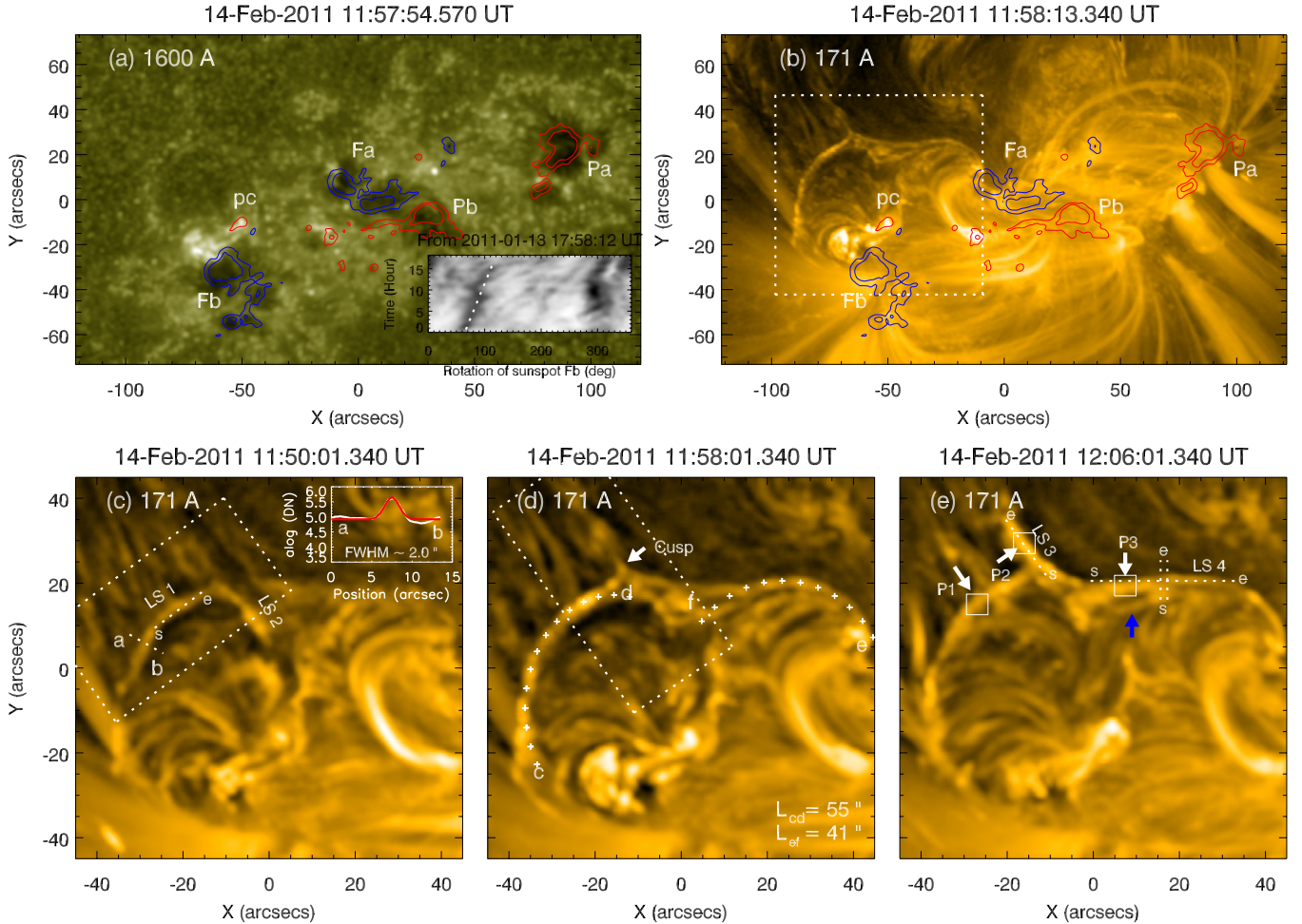


Figure 1. Images of AR NOAA 11158 and flaring coronal loops. Panels (a) and (b) show the entire maps of the AR in 1600 Å and 171 Å emissions, respectively. Red (blue) represents positive (negative) value of the longitudinal fields. The contour levels are $\pm 765, 1147$ G. Letters “P” and “F” mark the AR preceding and following polarities, respectively. The inset is a time slice showing the sunspot rotation, produced from an $r-\theta$ diagram of sunspot Fb. Panels (c)–(e) show 171 Å images, mapping the flaring loop region enclosed by the dotted square in (b). The inset shows the detrended intensities on the dotted line ab. The arc lines (plus sign) “cd” and “ef” delineate the profiles of the loops. The loop sections studied are indicated by LSs 1–4, and three of them, LSs 1, 2, and 3, are marked by the dotted lines with a starting point “s” and a terminal point “e.” This label way is the same for other similar lines. The white arrows point to the small white squares of P1, P2, and P3 on LSs 1, 3, and 4, respectively, where they are sampled to study the cause-and-effect connections of the QPPs. The loop temperatures and densities are also measured there.

(A color version of this figure is available in the online journal.)

In this paper, we utilize the 171 Å imaging observations of AIA, which have both the high spatial and temporal resolutions to study the medium QPPs in flaring coronal loops. We attempt to find out the mechanisms responsible for the observed QPPs. The subsequent sections are organized as follows. In Section 2, we discuss the observations, the data analysis, and its results. The possible implications of the results are discussed in Section 3.

2. OBSERVATIONS

The Helioseismic and Magnetic Imager (HMI) instrument (Schou et al. 2012) on board *SDO* obtains full solar disk images in the photospheric absorption line Fe I centered at the wavelength 6173.3 Å with spatial and temporal resolutions of $0''.5$ pixel $^{-1}$ and 45 s, respectively. The AIA instrument also takes full-disk images of the Sun in seven EUV channels and three UV-visible channels, whose spatial and temporal resolutions are $0''.6$ pixel $^{-1}$ and 12 s, respectively. AR NOAA 11158 was close to the disk center ($S19^\circ, W06^\circ$) when the 2011 February 14 C1.7 flare started at 11:51 UT, peaked at 12:00 UT, and ended at 12:26 UT in *GOES* soft X-ray flux. Throughout the flare period,

there were many QPPs appearing in the flaring loops above the eastern part of the AR. In this paper, we choose the images of the AR in the AIA 171 Å channel to study the above QPPs because it has an unprecedented signal-to-noise ratio that is excellent for studying transient and much fainter coronal features. Each image is smoothed over 3×3 pixels to match its actual $1''.5$ spatial resolution.

2.1. Morphology of AR NOAA 11158 and the Flare

AR NOAA 11158 has attracted much attention owing to the occurrence of a first X-class flare on 2011 February 15 in the rising phase of the current solar cycle 24. Detailed evolutions of the magnetic activities related to the flare have been extensively analyzed in many works (e.g., Maurya et al. 2012; Wang et al. 2012; Gosain 2012; Sun et al. 2012). Just before this X-class flare, the AR also produced at least one M-class and five C-class flares around its southeastern rotating sunspot, labeled Fb in Figures 1(a) and (b) of the 1600 Å and 171 Å images, respectively. The QPPs studied in this work are relevant to one of them, the C1.7 flare mentioned above. The bottom right inset of Figure 1(a) shows a time slice of the $r-\theta$ plot (Brown et al.

2003) obtained from the white-light images of HMI to measure the rotation of sunspot Fb. It shows that it rotated up to $\sim 60^\circ$ from 18:00 UT of February 13 to 12:00 UT of February 14, at a speed of $3^\circ 3 \text{ hr}^{-1}$. A long loop, resembling a complete unit enclosed by a dotted square in Figure 1(b), extended its left leg to sunspot Fb and its right leg to Fa, which was steady compared to Fb. In the following sections, we will see that the dynamic activities of Fb seem to exert more influence on the left leg than Fa does on the right leg.

In Figure 1(a), the 1600 Å brightening was adjacent to Fb, and in Figure 1(b), the corresponding 171 Å brightening was composed of a few small patches, which were located mainly at the tops and footpoints of some small loops connecting sunspots Fb and pc with the above-mentioned square in Figure 1(b). Their evolutions in 171 Å emission are shown in the bottom row of Figure 1.

2.2. Parameters of Flaring Coronal Loops

We are interested in the four loop sections marked by LSs 1 and 2 in Figure 1(c) and LSs 3 and 4 in Figure 1(e). Except for LS 2, the loops are marked by a dotted line with a starting point “s” and a terminal point “e.” During the flare, LS 1 and LS 4 developed quickly from vagueness to clarity marked by the arc lines (plus sign) “cd” and “ef” in Figure 1(d), respectively. LS 2 was greatly deformed, and a sharp cusp developed at its top, indicated by a white arrow. The cusp developed further and resembled an open flux tube, which is labeled LS 3 in Figure 1(e). However, at the moment we cannot determine whether LS 3 is coming from LS 1 or LS 4, or from both of them. In Section 2.7, the QPPs were found first appearing in LS 1, then in LS 3, and at last in LS 4. We speculate that LSs 1 and 4 might temporarily connect together and LS 3 might be a part of them.

All the loop sections basically had a similar width, and thus it seems reasonable to measure the width of one of them, e.g., a segment adjacent to LS 1. The inset of Figure 1(c) shows the detrended intensity (white) variation along line “ab,” and a Gaussian-function fitting (red) gives the loop width, $w \approx 2''$, just greater than the AIA spatial resolution of $1''.5$. At 11:58 UT, in Figure 1(d) we measure the lengths of loops of “cd” and “ef,” which are $L_{cd} = 55''$ and $L_{ef} = 41''$, respectively. The ratio of their mean length to width (assumed to be $2''$) is $L/w = 24$. The coronal loops may be unstable to a helical kink perturbation for long wavelengths, such as $48''$. To avoid the development of kink instabilities in the cylindrical plasma column, the condition $B_{0z}^2/B_\phi^2 > \log(\lambda/\pi R)$ has to be satisfied (Kruskal 1954; Shafranov 1957); here λ is the perturbation wavelength and R is the radius of the column. Substitutions of $48''$ for λ and $1''$ ($w = 2R$) for R give $B_{0z}^2/B_\phi^2 > 1.2$ for the loop stability. However, for magnetohydrostatic loops the force balance on the interface gives $p_0 + B_{0z}^2/2\mu = B_\phi^2/2\mu + p_e$, where p_0 (p_e) is the gas pressure inside (outside) the loop. The external pressure is the total one including gas and magnetic pressures. The typical ratios of external to internal density are $n_e/n_0 \approx 0.1\text{--}0.5$ inferred in the solar corona around oscillating loops (Aschwanden 2004). Furthermore, at 11:58 UT, the mean temperature T_0 around the loops was ~ 2.5 times that of the place far away from the loops (the background temperature T_e). Thus, B_{0z}^2/B_ϕ^2 may become less than 1, which was not satisfied by the above instability condition. Consequently, the kink instability might occur in the observed loops and produce the cusp (LS 3).

In Figure 1(e), we use an automated temperature and emission measure analysis of coronal loops developed by Aschwanden

Table 1
Physical Parameters of the Flaring Loops at 12:06 UT on 2011 February 14

	P1	P2	P3
Temperature (K) $\log(T_e)$	6.62 ± 0.03	6.63 ± 0.03	6.32 ± 0.08
Electron density (cm^{-3}) $\log(n_e)$	10.12 ± 0.01	10.20 ± 0.11	9.78 ± 0.15
Loop width (arcsec) w	2.05 ± 0.19	1.61 ± 0.39	2.17 ± 1.08
Acoustic speed (km s^{-1}) c_s^a	300	304	212

Note. ^a The acoustic speed in a fully ionized plasma is defined as $c_s = 147\sqrt{T_e/10^6} [\text{km s}^{-1}]$ (Aschwanden 2004).

et al. (2011), to detect the temperatures and densities in LSs 1, 3, and 4. The positions of doing measurements are highlighted by the white arrows and are labeled P1–P3. The derived parameters are listed in Table 1, and the acoustic speeds are included as well.

2.3. Flaring QPPs in LS 1

We first check LS 1 evolution in the period of 11:55:12–11:56:48 UT shown in Figures 2(a)–(e), and its field of view (FOV) is highlighted with a dotted rectangle in Figure 1(c). Evidently, LS 1 was made up of many bright blobs, whose spatial distribution exhibited periodicity (alternate changes of bright and dark spots). Two of them studied are shown by a dashed line (slice) in Figure 2(a), and their detrended intensity evolution (black) on this slice is shown in Figure 2(f). Hereafter, the y-axis of the same plots as Figure 2(f) or the following time–distance diagrams is set along the slice direction with a starting point “s” and a terminal point “e.” According to the dotted lines of Figure 2(f), the top blob moved downward at a speed of $v_m = 36 \text{ km s}^{-1}$, while the bottom one moved upward at $v_m = 42 \text{ km s}^{-1}$. The distances D between adjacent crests on the curve vary from 2.5 to 3.0 Mm for a sine-function fitting (red) shown in Figure 2(g). Clearly the two blobs approached each other, however, and the plasma in the loop was then possibly compressed.

Next, we make five cuts along LS 1 shown in Figure 2(b) to study the QPPs in LS 1. The distance of two adjacent cuts is 1 pixel ($0''.6$). We only utilize the spatial information of cuts 1 and 5 ($2''.4$ distance), and the rest are taken as reference. Their evolutions in the period of 11:40:00–12:35:24 UT are shown in Figures 3(a)–(e). The QPPs kept existing from the beginning to the end of the flare. Parts of them, in the three periods marked by slices 1–3 in Figure 3(a), are selected to study, as their evolution curves can be apparently fitted by a sine function with a time periodicity. From top to bottom, Figures 3(f)–(h) show the detrended intensities (black) and the fitting results (red) along slices 1–3. In Figure 3(f) (11:46:48–11:54:08 UT), from cut 1 to 5 we obtain a mean period of $P = 154$ s. The perturbations propagated downward from cut 5 to 1 (see the dotted lines). The phase delay between cuts 1 and 5 is $\delta P_{15} \sim 27$ s, the phase speed $v_P = 65 \text{ km s}^{-1}$ for a distance of $2''.4$, and then the wavelength $\lambda \approx 10 \text{ Mm}$ (here the QPPs were assumed to be MHD waves). The wavelength is about 3–4 times $D = 2.5\text{--}3.0 \text{ Mm}$, which is the distance between two adjacent blobs in Figure 2. From Figure 3(g) (12:01:24–12:04:24 UT), around the peak of the flare, the mean period was $P = 93$ s. However, there was no evident perturbation propagating along the loop possibly due to a short distance between cuts 1 and 5. From Figure 3(h) (12:22:12–12:27:12 UT), in the last period of the flare, the perturbation propagation exhibited an oscillation-like pattern, first upward at the speed of $v_P = 109 \text{ km s}^{-1}$ (from cut 1 to

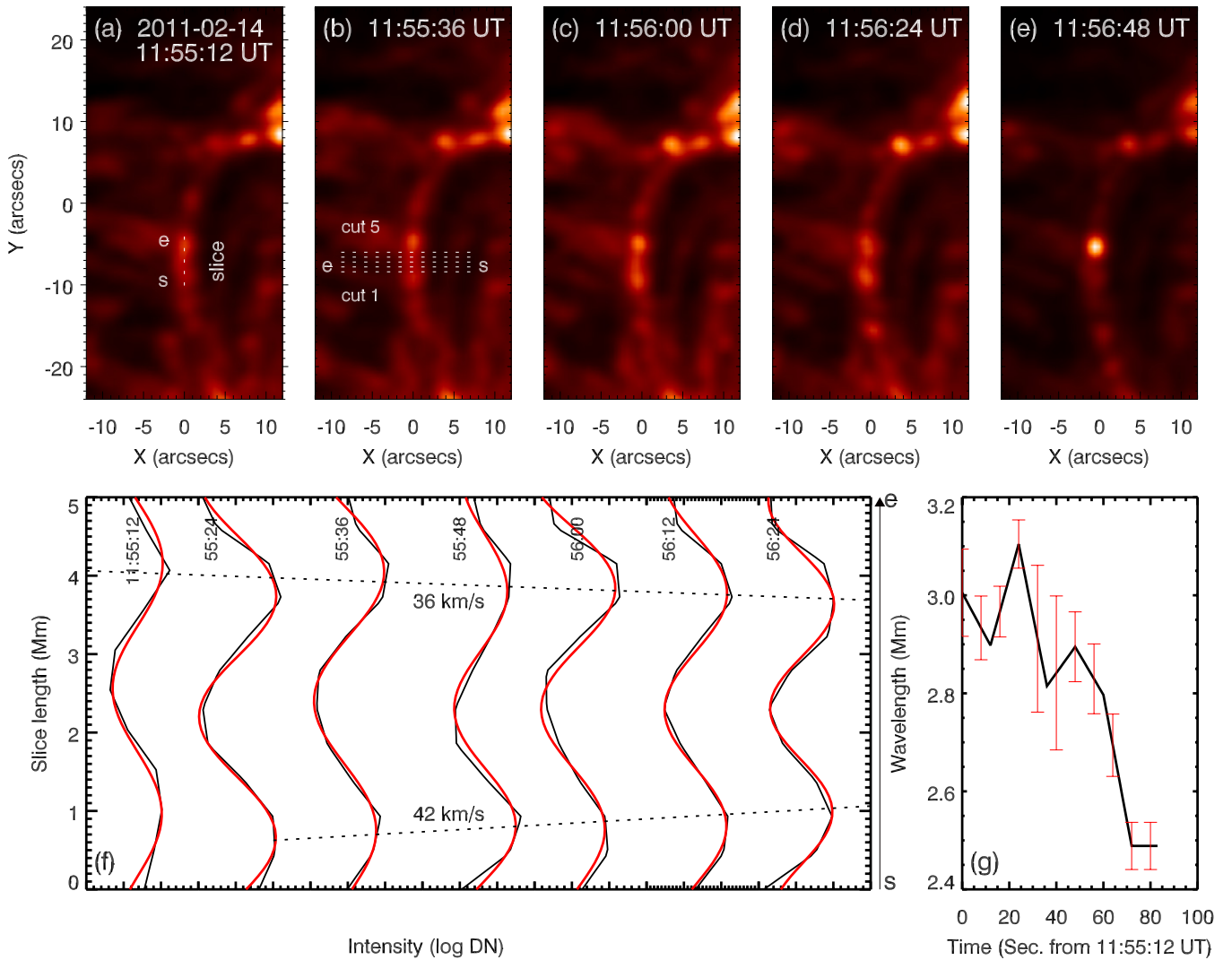


Figure 2. Spatial periodicity of LS 1 and its evolution. Its FOV, $24'' \times 48''$, has been marked by a dotted rectangle in Figure 1(c). Panels (a)–(e) show a temporal sequence of LS 1 in the period of 11:55:12–11:56:48 UT. Positions of the slice and cuts 1–5 are sampled to study the QPPs. Panel (f) shows the evolution of the detrended intensity along the slice, shown with the black lines. The sinusoidal fits, $A \sin(2\pi x/\lambda + \phi)$, to the curves are shown with the red lines. The dotted lines link the crests showing the spatial phase connection. The long black arrow close to the right edge of the panel indicates the starting (“s”) and terminal (“e”) points of the y-axis. The way of drawing the line in this panel is the same for the other similar plots. Panel (e) shows the evolution of the distance between two crests, which indicates the distance variations of the two adjacent blobs along the slice. The red error bar shows the fitting error.

(A color version of this figure is available in the online journal.)

5), then downward at 87 km s^{-1} (from cut 5 to 1), and finally stopping. The mean period was $P = 92 \text{ s}$.

2.4. Weak Perturbations in LS 2

A temporal sequence of LS 2, in the period of 11:53:48–11:55:24 UT, is shown in Figure 4 with a similar FOV as that of Figures 2(a)–(e), but rotated clockwise 10° . Similarly, to study the intensity evolution, we take a slice on LS 2, and the time series of the detrended intensities along it are shown in Figure 4(f). There were two blobs on the slice, the right one showing no movement while the left a slow rightward movement at a speed of $v_m = 3.5 \text{ km s}^{-1}$. The distance between the brightness peaks of two blobs varied and tended to decrease from $D \sim 3$ to 2.7 Mm in Figure 4(g). In sum, around the beginning of the flare there was no strong perturbation appearing in LS 2, and it was deformed greatly later (see Figure 1).

2.5. Flaring QPPs in LS 3

Similar to Figures 2 and 4, a temporal sequence of LS 3, in the period of 12:03:12–12:04:00 UT, is shown in Figure 5. The FOV is marked by a dotted rectangle in Figure 1(b). As above, we take a slice (dashed line) on LS 3 in Figure 5(a) to check its detrended intensity evolution shown in Figure 5(f). At first (12:03:12 UT), the perturbation changed violently and there was no evident phase relation available among the intensity curves. To check Figures 5(a)–(e), however, there was a bright blob linked by a blue dotted line ascending along the slice from 12:03:36 UT to 12:04:00 UT, which spanned three intensity peaks indicated by a blue dotted line in Figure 5(f). The moving velocity of the blob is $v_m = 76 \text{ km s}^{-1}$. From 12:04:12 UT, the perturbation became relatively stable. We could see the perturbation propagating upward along the slice, shown by the three black dotted lines. At a height of 1–2.5 Mm (projection height), the speed was $v_m = 21 \text{ km s}^{-1}$, moving higher it decreased to 9 km s^{-1} , and over that the perturbation vanished. The distance of two

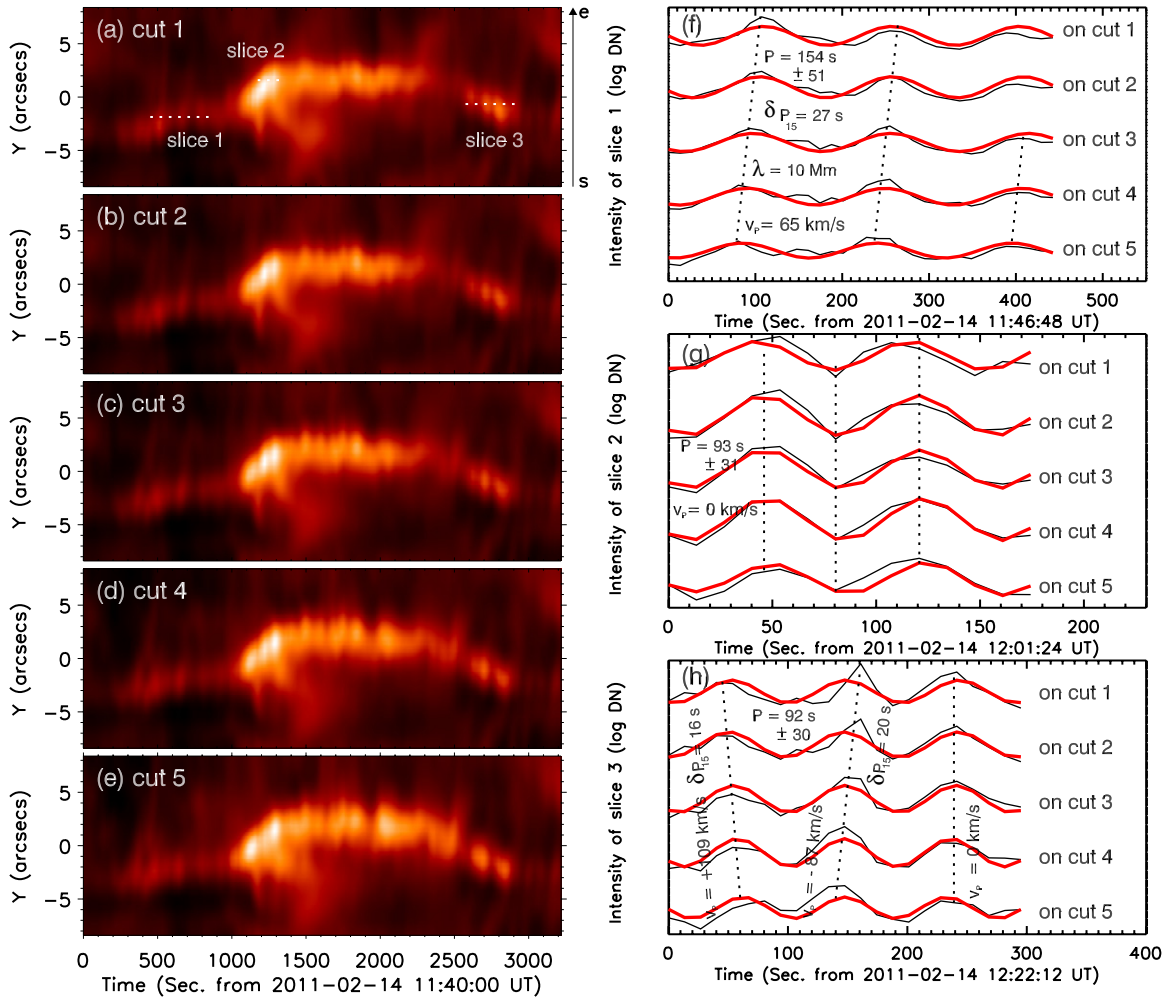


Figure 3. Flaring QPPs in LS 1. Time–distance diagrams of cuts 1–5 in Figure 2(b) are shown in (a)–(e), respectively. Slices 1–3 mark the periods in which the intensity variations of five cuts could be fitted with a sine function, $A \sin(2\pi t/P + \phi)$, which are shown in (f)–(h), respectively. The derived parameters are printed on the plots. The dotted lines thread the crests with temporal phase connections.

(A color version of this figure is available in the online journal.)

adjacent blobs shown in Figure 5(g) first experienced a fluctuation around $D = 4$ Mm, and then decreased to 3 Mm.

Similarly, in Figure 5(b) we make five cuts at an interval of a pixel ($0''.6$) on LS 3, whose time–distance diagrams are shown in Figures 6(a)–(e). There were at least five QPPs in the diagrams, but only the detrended intensity curves of the middle three could be easily fitted with a sine function. Because of the different time intervals for the three QPPs, we use slice 1 marking the first and second ones and slice 2 marking the second and the last ones shown in Figure 6(a). Figures 6(f) and (g) show their intensity evolutions and the corresponding fitting curves of cuts 1–5. The perturbations propagated upward from cut 1 to 5, and the phase relation among them was evident, indicated by the dotted lines. Based on Figure 6(f) (12:02:48–12:06:12 UT), a mean period of $P = 93$ s from cut 1 to 5 is found. The phase delay δP_{51} between cuts 5 and 1 was 18 s, and then the propagating speed is obtained for a distance of $2''.4$, $v_p \sim 97$ km s $^{-1}$. Therefore, the perturbation wavelength λ is 9.6 Mm. Note that this QPP propagating with a velocity of 97 km s $^{-1}$ should connect to the above blob moving at the velocity $v_m = 76$ km s $^{-1}$ in Figure 5. It thus indicates that in this case the QPP possibly resulted from the blob moving along the loop. Similarly, from Figure 6(g) (12:04:24–12:07:12 UT), we find the mean period from cut 1 to 5, $p = 112$ s, which was slightly larger than the previous

period (99 s). The phase speed and perturbation wavelength were $v_p = 73$ km s $^{-1}$ and $\lambda = 8.0$ Mm, respectively. Again, we find that these two wavelengths were greater than the distance $D \approx 4$ Mm of two adjacent blobs along the slice in Figure 5. The wavelengths were roughly 2 times the distance D .

2.6. Flaring QPPs in LS 4

We make three cuts on LS 4 in Figure 1(e), the horizontal one superposing with LS 4, and the other two (separated by $2''.4$) perpendicular to LS 4 at its middle position. Figures 7(a) and (b) show time–distance diagrams of two vertical cuts, in which no discernible QPPs can be found until at about 12:02:12 UT (400 s in the x-axis and $-3''$ in the y-axis). We make slices 1 and 2 on them and plot the detrended intensities in Figure 7(d). Sinusoidal fits to the temporal profiles yield a mean period of $P = 32$ s. However, there was no phase relation found between the two profiles, possibly due to the short distance between them ($2''.4$). In comparison with Figure 1(e), we find that these intensity oscillations should come from a loop adjacent to LS 4 from below highlighted by a blue arrow. Figure 7(c) shows the time–distance diagram of the horizontal cut along LS 4. We find two QPPs, wave-like trains, propagating downward along the loop onset at about 12:03:36 UT, on which three slices are

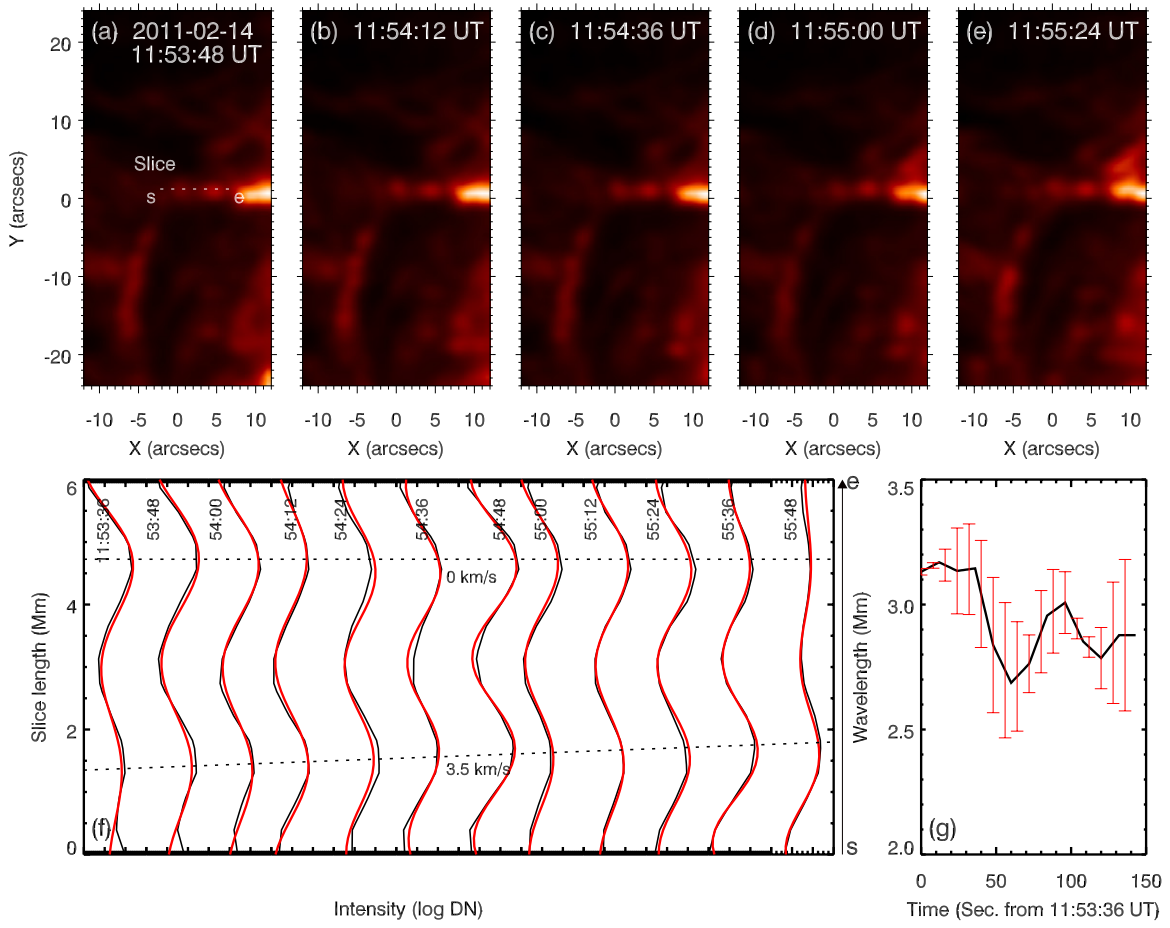


Figure 4. Same as Figure 2, but for LS 2.
(A color version of this figure is available in the online journal.)

made to study their detrended intensities shown in Figure 7(e). Sinusoidal fits to these profiles yield a mean period of $P = 24$ s. From the evident phase relation among the three profiles, we obtain a mean velocity of $v_P = 235 \text{ km s}^{-1}$ and wavelength of $\lambda = 5.6 \text{ Mm}$. Besides, there were still other ones appearing along with or following up the two QPPs at a propagating velocity of $v_P = 128 \text{ km s}^{-1}$, and the ones before them at a velocity of $v_P = 80 \text{ km s}^{-1}$ onset at 11:56:24 UT.

To further study the QPPs in LS 4, we plot the temporal sequence of LS 4 in Figure 8. To enhance intensity comparison, each image has been subtracted from a smoothed image created from itself. Along two black arrows, we find for two times the bright blob moving toward the loop footpoint at a speed of $v_m = 182 \text{ km s}^{-1}$, which should correspond to the above two wave-like trains in Figure 7(c). Moreover, the time interval between blobs p11 and p12 (p21 and p22), connected by a white dotted line, is just 24 s, the same as that in Figure 7(e). On the one hand, this evidence confirms that the 24 s period was not the artifact caused by the Nyquist frequency of the AIA 12 s cadence. On the other hand, it further confirms that the QPP resulted from the bright-blob shifting. In addition, the distributions of the bright blobs in LS 4 and its adjacent loop below, highlighted by the white arrows in Figures 8(c) or (g), were with a spatial periodicity. Roughly estimating the distances between any two adjacent blobs in LS 4 and its adjacent one, we find they were $D \sim 3''6$ (2.6 Mm) and $D \sim 4''2$ (3.0 Mm), respectively. Once again, the perturbation wavelength $\lambda = 5.6 \text{ Mm}$ was two times the distance $D = 2.6(3.0) \text{ Mm}$.

2.7. Temporal Connections among the Flaring QPPs

In the above sections, we have found many QPPs in LSs 1, 3, and 4. We would like to know how they are connected to each other in this C1.7 flare. To this end, we select three areas on LSs 1–3 to study with an FOV of $6'' \times 6''$ marked by the three squares in Figure 1(e), where are also the positions of P1–P3 selected to detect the loop temperatures and densities. Variations of the mean intensities in the three squares and the GOES X-ray flux in 1–8 Å are plotted in Figure 9. In Figure 9(a), the maximum peaks of the P1 curve and the GOES flux simultaneously appeared at around 12:00 UT, and those of the P2 and P3 curves appeared later at around 12:05 UT. By shifting the data of P2 and P3 3.6 and 3.2 minutes ahead, respectively, we find that the correlation coefficient between P1 and P2 was up to the maximum 0.86, P1 and P3 0.67, and P2 and P3 0.83 in the period of 11:56–12:10 UT. The shifted data are shown in Figure 9(b). It shows that the individual peaks of P1 and P2 were in phase with a period of $P \sim 90$ s, and those of P2 and P3 with $P \sim 180$ s. However, it is difficult to determine the direct connections between P1 and P3 from their individual peak positions. After all, the correlation between them was weakest among the three curves. In sum, the QPPs in LSs 1–3 were all closely associated with the flare, but a slight difference is that those in LS 1 are in phase with the peak of the flare, whereas those in LSs 3 and 4 show a ~ 5 minute delay.

To further find out their connections, we put together in Figure 10 the time–distance diagrams along LSs 1, 3, and 4

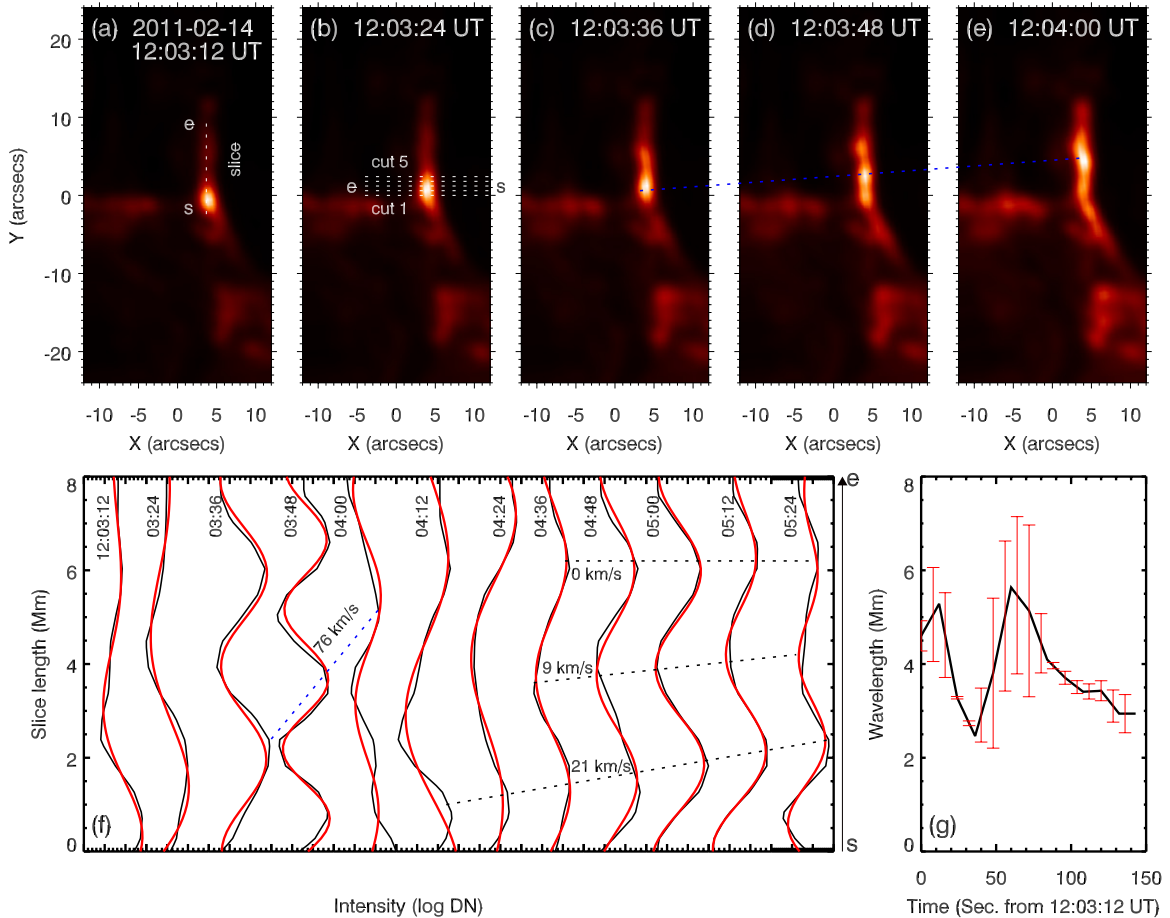


Figure 5. Same as Figure 2, but for LS 3. Its FOV, $24'' \times 48''$, has been marked by a dotted rectangle in Figure 1(d). The blue dotted line threads an upward-moving bright blob in (c)–(e). Its motion at a speed of 76 km s^{-1} is also marked by another dotted blue line in (f).

(A color version of this figure is available in the online journal.)

In Figures 1(c) and (e). Three black dotted lines mark the start, peak, and end times of the flare. About 6 minutes before the flare (300 s position), the QPPs first appeared in LS 1 propagating downward at a speed of $v = 62 \text{ km s}^{-1}$. This is basically consistent with the analysis of the QPPs in Figure 3(e), where we have found their mean period, $P = 154 \text{ s}$ (~ 3 minutes). Three-minute oscillations before the flare burst were interpreted as slow magnetoacoustic waves propagating from a sunspot along coronal loops upward to the flare site and causing the energy release (Sych et al. 2009; Abramov-Maximov et al. 2012). In our case, although the QPPs with periods of ~ 3 minutes appeared before the flare, their propagating direction along LS 1 was downward rather than upward. About 3 minutes before the peak (1000 s position), many more QPPs appeared in LS 1, fewer (with a propagating speed of $v = 80 \text{ km s}^{-1}$) in LS 4, while nearly nothing in LS 3 (the signals were weak). Similar to Figure 3(f), we find that the intensity oscillations only appeared in LS 1, which did not propagate around the flare peak. About 5 minutes later (1300 s position), a large number of them began to appear in LS 3, which propagated upward at a speed of $v = 108 \text{ km s}^{-1}$ ($P = 99\text{--}112 \text{ s}$ in Figure 6). About 7 minutes later (1420 s position), a lot of QPPs began to appear in LS 4, propagating downward first at a fast speed of 235 km s^{-1} and then at a slow speed of 128 km s^{-1} . In Figure 7, we have found the mean period of the QPPs ($v = 235 \text{ km s}^{-1}$), $P = 24 \text{ s}$. Such short periods are also found in LSs 1 and 3, for instance, a 32 s period in panel (a) and a 24 s period in panel (b), shown by

the insets. The blue lines are the sinusoidal fits to the detrended intensity profiles along slices 1 and 2.

Around the end of the flare, there were many QPPs appearing in LS 1 again. Some of them were propagating up and down and vanished at 12:27:12 UT in Figure 3(g). In Figure 1(b), we have known the footprint of LS 1 extended to the rotating sunspot Fb, and its dynamic activities may exert influence on the QPPs in LS 1, for instance, producing the QPPs or modulating their periods, etc. The up and down propagations of the QPPs may also be related to the sunspot activities. On the other hand, there were nearly no QPPs appearing in LS 4, whose footprint connected with a relatively stable sunspot Fa.

Figures 10(d)–(e) are the fast Fourier transform (FFT) of the averaged intensities over the entire spatial scales of Figures 10(a)–(c), respectively. Each profile has been smoothed over a three-point bin. The Nyquist frequency of the AIA 12 s cadence is marked by a black dotted line. Around this frequency, we do find the real QPPs with periods of ~ 24 s and 32 s in the three loop sections. We also find the long QPPs with periods of 95 s and 166 s in LS 1 and 95 s and 112 s in LS 3. The remarkable periods of LS 4 in the FFT plot were 35 s, 67 s, and 166 s. However, the medium QPPs with periods of ~ 60 s are not detected in the time-distance diagrams of LSs 1–3.

3. DISCUSSION

In this work, we present detailed AIA 171 Å observations of the QPPs in four loop sections, LSs 1–4, over the eastern part of

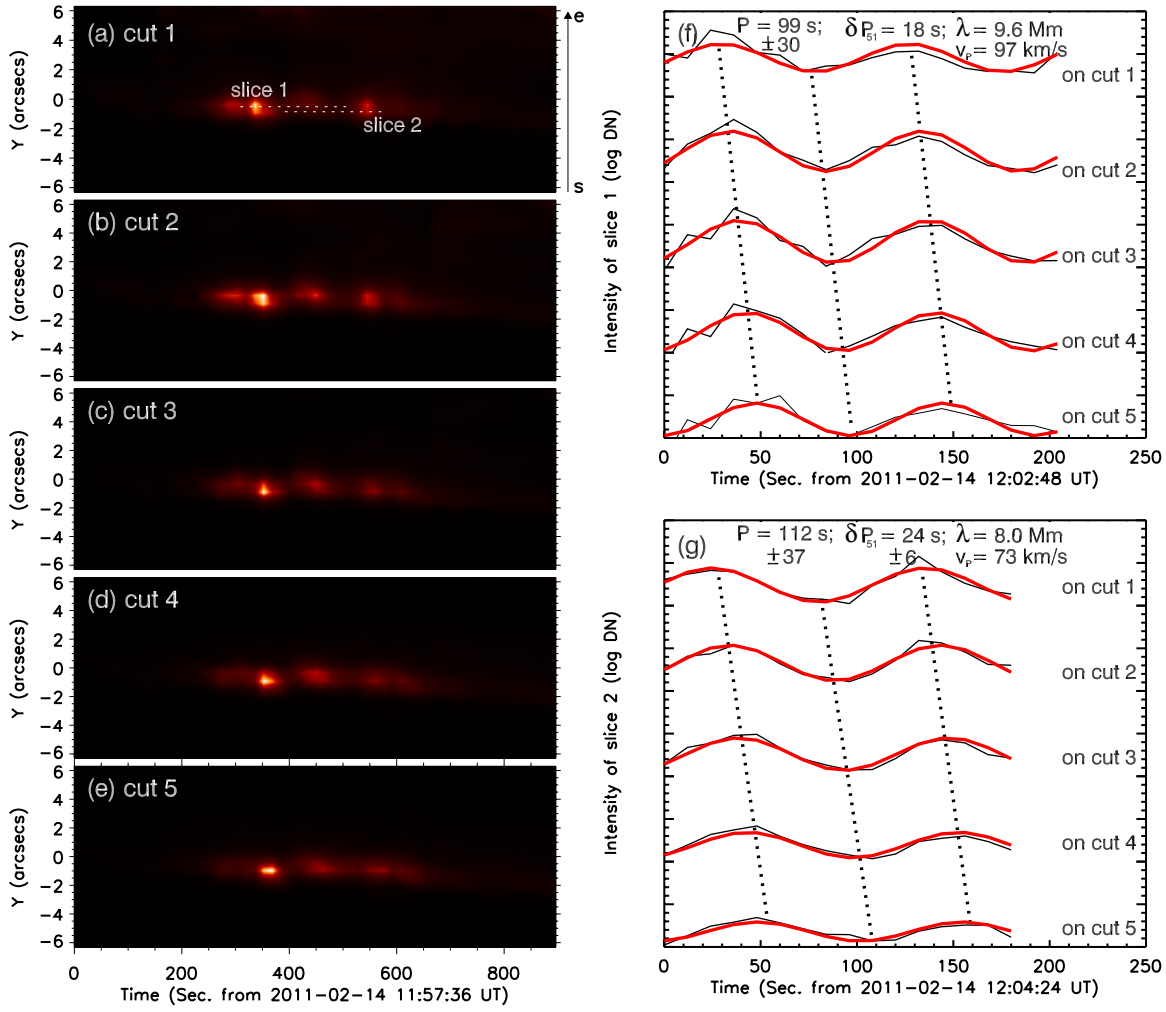


Figure 6. Same as Figure 3, but for LS 3.
(A color version of this figure is available in the online journal.)

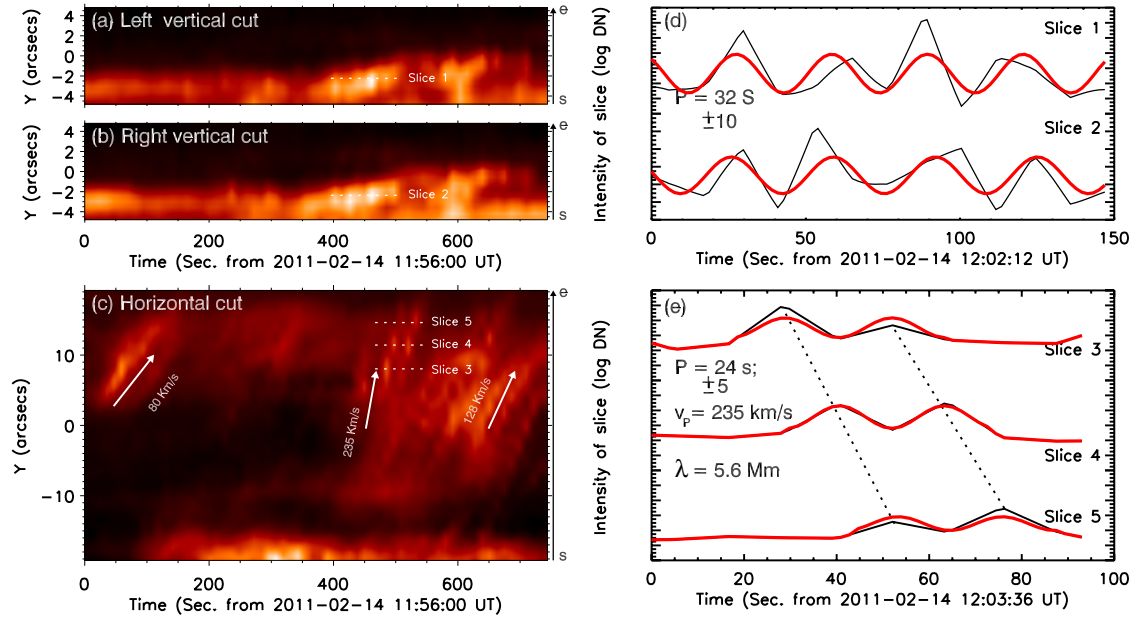


Figure 7. Flaring QPPs in LS 4. Panels (a)–(c) show time–distance diagrams of the vertical and horizontal cuts of LS 4, respectively. The vertical cuts are perpendicular to the dotted line marking LS 4 at its middle position in Figure 1(e), and the horizontal one superposes it. The white arrows mark three perturbations propagating downward along LS 4, at speeds of 80 km s^{-1} , 235 km s^{-1} , and 128 km s^{-1} , respectively. Panels (d)–(e) show the intensity evolutions along slices 1–5 and their sinusoidal fitting results.

(A color version of this figure is available in the online journal.)

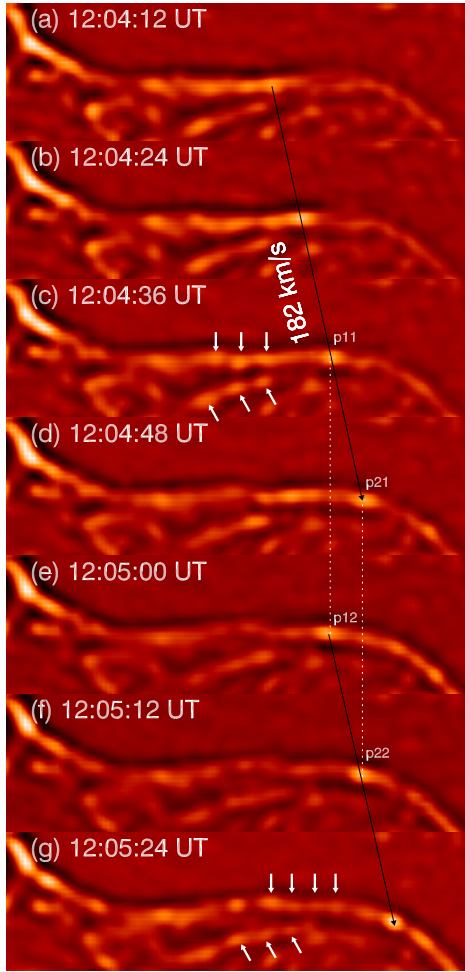


Figure 8. Temporal sequence of LS 4. The long black arrows mark bright blobs propagating downward along the loop for two times, and the short white ones mark the loop segments with evident spatial periodicity. The white dotted line threads the bright blobs of p11 and p12 (p21 and p22).

(A color version of this figure is available in the online journal.)

AR NOAA 11158 during the 2011 February 14 C1.7 flare. The main observations are summed up as follows:

1. The footpoints of LSs 1 and 3 connected with a fast rotating and a relatively stable sunspot, respectively. The flare occurred near the rotating sunspot. LS 3 was a cusp protruding from the top of LS 2. We find the apparent QPPs in all the loop sections except LS 2. The QPPs in LS 1 appeared 6 minutes before the flare, around the peak and the end of the flare. However, most QPPs in LSs 3 and 4 are found after the peak of the flare, and there was a 5–7 minute delay for their appearance relative to those in LS 1. After reducing the delays, the correlation between the QPPs in LSs 1 and 3 is up to 86%, and it decreases slightly to 83% between those in LSs 2 and 3.
2. All the observed loop sections were made up of bright blobs exhibiting evident spatial periodicity (alternately bright and dark change in intensity). The distance of two adjacent bright blobs along a loop ranged between 2.4 and 5.0 Mm. More often, they moved at a speed of $v_m = 3\text{--}40 \text{ km s}^{-1}$, slower than the perturbation propagating velocity of the QPPs, $v = 60\text{--}200 \text{ km s}^{-1}$, which was then smaller than the acoustic speed in the loops, $v_s = 200\text{--}300 \text{ km s}^{-1}$.
3. The QPP periods were from 24 to 166 s. The shortest and longest periods are detected from the time–distance diagrams, and the medium periods, such as $P \approx 60 \text{ s}$, by the FFT method. Based on the time–distance diagrams, we also find the perturbation wavelength of the QPPs to be $\lambda = 5\text{--}10 \text{ Mm}$ (as if they were MHD waves), which were 2–4 times the distance $D = 2.4\text{--}5.0 \text{ Mm}$ of two adjacent bright blobs along a loop.

Based on the observational facts, speculations about the possible causes of the flaring QPPs are as follows. First, the short QPPs with periods of $P = 24 \text{ s}$ in LS 4 could be attributed to sausage-mode oscillations. The non-leaky sausage-mode oscillations in loops can exist only if their longitudinal wave numbers are greater than the cutoff value, which imposes a constraint on the possible loop density and geometry for the

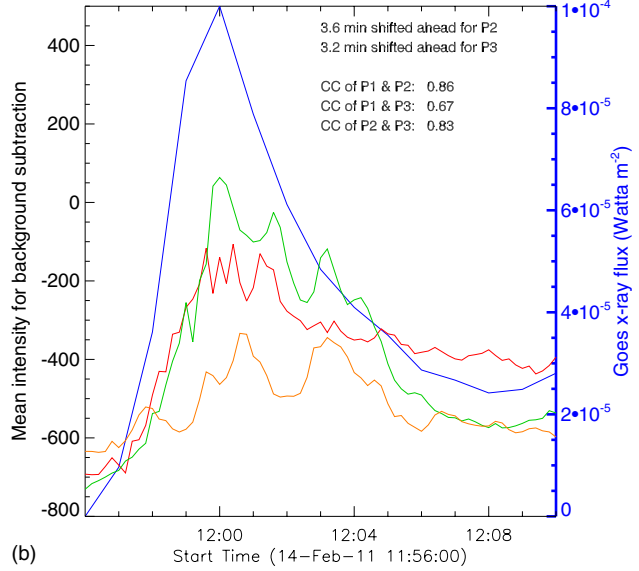
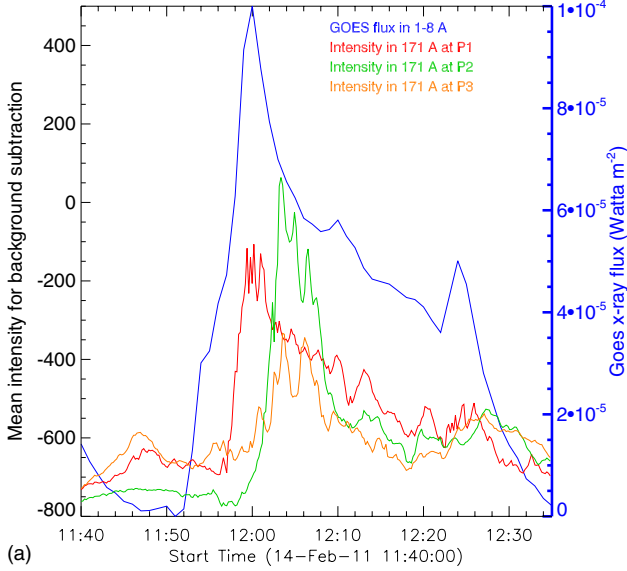


Figure 9. Evolutions of the mean intensities in the small squares ($6'' \times 6''$ FOV) marked by P1–P3 in Figure 1(e). The blue line is for the GOES X-ray flux in 1–8 Å, and the red, green, and brown ones for the intensity profiles of P1, P2, and P3, respectively. Panel (a) covers the whole period of the flare, of which a segment, around the flare peak of the flare (12:00 UT), is shown in (b).

(A color version of this figure is available in the online journal.)

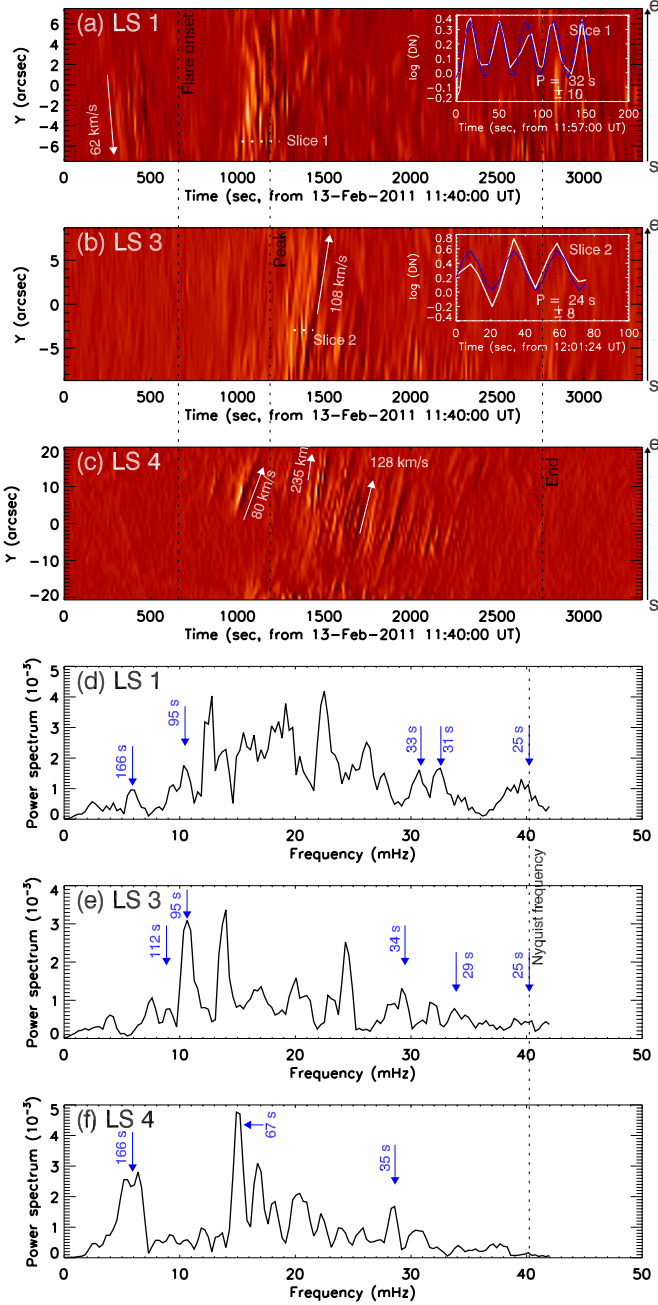


Figure 10. Temporal connections among the QPPs in the flaring loops. Panels (a)–(c) show time–distance diagrams of the dashed lines along LSs 1, 3, and 4 in Figures 1(c) and (e). Three vertical dashed lines mark the start, peak, and end times of the flare. The long white arrows highlight the propagating QPPs along the loops. The insets in (a) and (b) show the detrended intensities (white) along slices 1 and 2, respectively, to which the sinusoidal fits are shown by the blue lines. Panels (d)–(f) show FFT to the averaged intensities over the whole widths of (a)–(c), respectively.

(A color version of this figure is available in the online journal.)

fundamental sausage mode, $n_i > 2.334n_e(L/w)^2$ (Aschwanden 2004). Here, the subscripts i and e refer to the density inside and outside a loop, respectively. Given $L = 48''$, $w = 2''$, the typical coronal density is $n_e = 10^8 \text{ cm}^{-3}$, and then the above inequality becomes $n_i > 1.3 \times 10^{11} \text{ cm}^{-3}$. Evidently, the derived densities listed in Table 1 are one order less than the above value for trapping any non-leaky fundamental sausage mode. However, for low-density ($n_e < 10^{10} \text{ cm}^{-3}$) loops, a small segment of them may host the sausage oscillations of

high harmonic ($N \gg 1$) nodes (Aschwanden et al. 2004). In our case, the actual excited mode should be as high as up to $N = 10$ ($\lambda = 2L/N$) to match the velocity of 235 km s^{-1} in LS 4. But it is difficult to explain why only a very high mode is excited (Melnikov et al. 2005). Nevertheless, if the wavelength is longer than the cutoff, sausage waves do not cease to exist. They become leaky, and the leakage may take several periods of oscillations (Pascoe et al. 2007). Therefore, sausage perturbations with a wavelength longer than the cutoff or those of high harmonics only confined to a small loop segment could not be ruled out as an explanation for the 24 s QPPs in LS 4. These discussions may be applied to the other short periods in LSs 1 and 3 as they were interconnected as shown in Figures 9 and 10.

Second, the plasma density in the loops could vary in response to the modulation of slow magnetoacoustic waves. That is, the observed QPPs with periods of $P > 60$ s may be explained as the slow magnetoacoustic waves in the loops. In Figures 2, 4, and 5, the spatial distance variations of two bright blobs along the loops possibly reflect compression and expansion of the plasma. Moreover, their propagating velocity in the range $60\text{--}200 \text{ km s}^{-1}$ was smaller than but close to the acoustic speed v_s , which was about $200\text{--}300 \text{ km s}^{-1}$. We take the loop lengths of LS 1(4) and LS 3 as $L_1 = 48''$ and $L_2 = 16''$, respectively. In LS 1, for the QPPs with periods of 154 s and 92 s, the excited acoustic mode can be as high as up to $N \approx 6$ to fit their propagating velocities of 70 and 100 km s^{-1} , respectively. In LS 3, for the QPPs with periods of ~ 106 s and $v = 85 \text{ km s}^{-1}$, N decreases to about 3. In LS 4, for the QPPs with periods of 166 s and $v = 80 \text{ km s}^{-1}$, the excited mode is $N \approx 5$, and in the case of $v = 128 \text{ km s}^{-1}$, N becomes about 3. Therefore, if the observed QPPs are the slow magnetoacoustic waves, the waves would be the high-order harmonic, for instance, at least $N = 3$. Nakariakov et al. (2004) suggested that the QPPs with periods in the range 10–300 s, frequently observed in flaring coronal loops in the radio, visible light, and X-ray bands, may be produced by the second standing harmonic of the acoustic mode. Similarly, the QPPs we observed with periods of $P > 60$ s may be ascribed to the higher modes of the acoustic waves, e.g., the third or fourth harmonic. The discussions are available to the short QPPs with periods of 24 s (32 s) as well.

Furthermore, a common wave has a property with both temporal and spatial periodicities. This is not limited to slow magnetoacoustic waves. The observed QPPs possessed the common properties of a wave. But the wavelength obtained from the temporal sequence of a loop section was not equal to that from the time–distance diagram. For example, in Figure 2(g) we find that the distance D of two adjacent blobs ranged between 2.5 and 3.0 Mm, and the moving velocity v_m between 36 and 42 km s^{-1} , whereas the perturbation wavelength was $\lambda = 10 \text{ Mm}$ in Figure 3(f), and the propagating velocity $v_P = 65 \text{ km s}^{-1}$. The ratio of the wavelength to the adjacent blob distance was $\lambda/D = 3\text{--}4$, and the velocity ratio $v_P/v_m \approx 2$. Even if the two velocities were close, there was still an undeniable difference in length. For example, the moving velocity in Figure 5(f) was $v_m = 76 \text{ km s}^{-1}$ in the period of 03:36–04:00 UT, being nearly equal to that in Figure 6(g), $v_P = 97 \text{ km s}^{-1}$, but the length ratio was still up to $\lambda/D \approx 2$ estimated from Figures 5(g) and 6(g). This was the same for LS 4. How to explain this gap? It is possible that there was the second/third harmonic of the acoustic waves with a wavelength being $(1/2)/(1/3)$ of $\lambda = 10 \text{ Mm}$, but we could not detect them with the present methods.

Note that in the discussions above, we do not take into account the projection effect. If one considers an inclined coronal loop, the detected propagating speeds of the QPPs in it will be magnified by $1/\cos\theta$ (where θ is the inclination angle), which may help explain the difference between the observed and estimated speeds of slow magnetoacoustic waves (e.g., de Moortel 2009) and may also degrade the estimated harmonic order, e.g., from $N > 5$ down to 3 or 4 (or even lower). Finally, the possible cause of the QPPs could be a quasi-periodic regime of the energetic electron acceleration/injection in the loop generated by magnetic reconnection (Tajima et al. 1987; Kliem et al. 2000; Ofman & Sui 2006), which is known as load/unload models by Nakariakov & Melnikov (2009). The models explain QPP as a side effect of transient energy releases, in particular of magnetic reconnection. The observed periodic behavior is considered to be rather accidental, connected with the relationship between energy load and unload balance.

This work is supported by the AJFC project (Nos. 10878016 and 11073050), the Young Researcher Grant of National Astronomical Observatories, Chinese Academy of Sciences (CAS), the Key Laboratory of Solar Activity of CAS, and the National Basic Research Program of China under grant 2011CB8114001. We are grateful to Drs. W. Liu, H. Zhao, and to the anonymous referee for valuable comments.

REFERENCES

- Abramov-Maximov, V. E., Gelfreikh, G. B., & Shibasaki, K. 2012, *Sol. Phys.*, **273**, 403
- Asai, A., Shimojo, M., Isobe, H., et al. 2001, *ApJ*, **562**, L103
- Aschwanden, M. J. 1987, *Sol. Phys.*, **111**, 113
- Aschwanden, M. J. 2003, arXiv:[astro-ph/0309505](http://arxiv.org/abs/astro-ph/0309505)
- Aschwanden, M. J. 2004, Physics of the Solar Corona (Chichester: Springer)
- Aschwanden, M. J., Boerner, P., Schrijver, C. J., & Malanushenko, A. 2011, *Sol. Phys.*, 384
- Aschwanden, M. J., Nakariakov, V. M., & Melnikov, V. F. 2004, *ApJ*, **600**, 458
- Banerjee, D., Teriaca, L., Gupta, G. R., et al. 2009, *A&A*, **499**, L29
- Berghmans, D., & Clette, F. 1999, *Sol. Phys.*, **186**, 207
- Brown, D. S., Nightingale, R. W., Alexander, D., et al. 2003, *Sol. Phys.*, **216**, 79
- de Moortel, I. 2009, *Space Sci. Rev.*, **149**, 65
- Foullon, C., Verwichte, E., Nakariakov, V. M., & Fletcher, L. 2005, *A&A*, **440**, L59
- Gosain, S. 2012, *ApJ*, **749**, 85
- Inglis, A. R., & Nakariakov, V. M. 2009, *A&A*, **493**, 259
- Inglis, A. R., Nakariakov, V. M., & Melnikov, V. F. 2008, *A&A*, **487**, 1147
- Jakimiec, J., & Tomczak, M. 2008, *Cent. Eur. Astrophys. Bull.*, **32**, 65
- King, D. B., Nakariakov, V. M., Deluca, E. E., Golub, L., & McClements, K. G. 2003, *A&A*, **404**, L1
- Kliem, B., Karlický, M., & Benz, A. O. 2000, *A&A*, **360**, 715
- Kruskal, M. D. 1954, U. S. Atomic Energy Commission Report No. NYO-6015
- Kupriyanova, E. G., Melnikov, V. F., Nakariakov, V. M., & Shibasaki, K. 2010, *Sol. Phys.*, **267**, 329
- Lemen, J. R., Title, A. M., Akin, D. J., et al. 2012, *Sol. Phys.*, **275**, 17
- Li, Y. P., & Gan, W. Q. 2008, *Sol. Phys.*, **247**, 77
- Liu, W., Title, A. M., Zhao, J., et al. 2011, *ApJ*, **736**, L13
- Marsh, M. S., Walsh, R. W., & Plunkett, S. 2009, *ApJ*, **697**, 1674
- Maurya, R. A., Venkatesdy, P., & Ambastha, A. 2012, *ApJ*, **747**, 134
- McAteer, R. T. J., Gallagher, P. T., Brown, D. S., et al. 2005, *ApJ*, **620**, 1101
- McIntosh, S. W., de Pontieu, B., & Tomczyk, S. 2008, *Sol. Phys.*, **252**, 321
- Melnikov, V. F., Reznikova, V. E., Shibasaki, K., & Nakariakov, V. M. 2005, *A&A*, **439**, 727
- Mészárosová, H., Karlický, M., Rybák, J., Fárník, F., & Jiřička, K. 2006, *A&A*, **460**, 865
- Nakariakov, V. M., Foullon, C., Myagkova, I. N., & Inglis, A. R. 2010, *ApJ*, **708**, L47
- Nakariakov, V. M., Foullon, C., Verwichte, E., & Young, N. P. 2006, *A&A*, **452**, 343
- Nakariakov, V. M., & Melnikov, V. F. 2009, *Space Sci. Rev.*, **149**, 119
- Nakariakov, V. M., Melnikov, V. F., & Reznikova, V. E. 2003, *A&A*, **412**, L7
- Nakariakov, V. M., Tsiklauri, D., Kelly, A., Arber, T. D., & Aschwanden, M. J. 2004, *A&A*, **414**, L25
- Ofman, L., Romoli, M., Poletto, G., Noci, G., & Kohl, J. L. 1997, *ApJ*, **491**, L111
- Ofman, L., & Sui, L. 2006, *ApJ*, **644**, L149
- Pascoe, D. J., Nakariakov, V. M., & Arber, T. D. 2007, *A&A*, **461**, 1149
- Rao, A. R., Malkar, J. P., Hingar, M. K., et al. 2010, *ApJ*, **714**, 1142
- Reznikova, V. E., Melnikov, V. F., Su, Y., & Huang, G. 2007, *Astron. Rep.*, **51**, 588
- Schou, J., Scherrer, P. H., Bush, R. I., et al. 2012, *Sol. Phys.*, **275**, 229
- Shafranov, V. D. 1957, *J. Nucl. Energy III*, **5**, 86
- Sun, X., Hoeksema, J. T., Liu, Y., et al. 2012, *ApJ*, **748**, 77
- Sych, R., Nakariakov, V. M., Karlický, M., & Anfinogentov, S. 2009, *A&A*, **505**, 791
- Tajima, T., Sakai, J., Nakajima, H., et al. 1987, *ApJ*, **321**, 1031
- Tan, B., Zhang, Y., Tan, C., & Liu, Y. 2010, *ApJ*, **723**, 25
- Wang, S., Liu, C., Liu, R., et al. 2012, *ApJ*, **745**, L17
- Wang, T. J., Ofman, L., Davila, J. M., & Mariska, J. T. 2009, *A&A*, **503**, L25
- Zimovets, I. V., & Sturinsky, A. B. 2009, *Sol. Phys.*, **258**, 69